ACS APPLIED ENERGY MATERIALS

Open Access

This article is licensed under CC-BY 4.0

www.acsaem.org

Article

Interfacial Chemistry between Formamidinium Lead Trihalide Perovskites and Atomic-Layer-Deposited Tin Oxide

Bhavya Rakheja,* Adam Hultqvist, Rahul Mahavir Varma, Natalia M. Martin, Karen Radetzky, Stefania Riva, Evelyn Johannesson, Ute B. Cappel, Håkan Rensmo, Erik M. J. Johansson, and Tobias Törndahl

Cite This: *ACS Appl. Energy Mater.* 2025, 8, 8467−8478

Read Online

ACCESS | Metrics & More | Article Recommendations | Supporting Information

ABSTRACT: Tin oxide (SnO_x) by atomic-layer deposition (ALD), in combination with fullerene, is widely employed as an electron transport layer in p−i−n perovskite solar cells. This study investigates the direct deposition of ALD SnO_x on top of formamidinium (FA)-based perovskites, as a step toward the elimination of the fullerene interlayer and its poor effect on solar cell's long-term stability. The interfacial chemistry between FA-based perovskites ($FAPbI_3$ and $FAPbBr_3$) and ALD SnO_x was studied using soft and hard X-ray photoelectron spectroscopy (SOXPES and HAXPES) with a focus on investigating the separate roles FA and different halides play during interface formation. $FAPbI_3$ and $FAPbBr_3$ solar cell structures solely containing ALD SnO_x resulted in s-shaped current−voltage characteristics, indicating the formation of a transport barrier at the interface. Both SOXPES and HAXPES measurements revealed the emergence of additional nitrogen states at the interface during the ALD SnO_x deposition on $FAPbI_3$ and $FAPbBr_3$, where these states are linked to the decomposition of FA^+. The $FAPbI_3$/ALD SnO_x interface also showed the presence of lead iodide (PbI_2) through additional lead states other than that from $FAPbI_3$ by using SOXPES measurements. Concerning the $FAPbBr_3$/ALD SnO_x interface, no additional lead states were observed; however, measurements instead revealed the formation of Sn−Br bonds at the interface along with the migration of bromine ions into the bulk of the ALD SnO_x. Thus, $FAPbI_3$ and $FAPbBr_3$ undergo distinct reaction pathways upon direct deposition of ALD SnO_x on top of them. We reason that the decomposition of FA^+ in both perovskites and the formation of PbI_2 at the $FAPbI_3$/ALD SnO_x interface and the incorporation of Br in SnO_x at the $FAPbBr_3$/ALD SnO_x interface prove detrimental toward device performance. Therefore, careful interfacial engineering that can mitigate the formation of these products should be utilized to enhance the performance of perovskite solar cells.

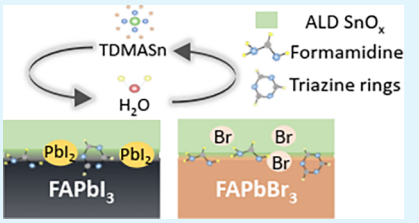

KEYWORDS: *atomic-layer deposition, interfacial chemistry, X-ray photoelectron spectroscopy, perovskite solar cell, precursor chemistry, tin oxide*

Downloaded via UPPSALA UNIV on September 8, 2025 at 11:37:39 (UTC).
See https://pubs.acs.org/sharingguidelines for options on how to legitimately share published articles.

INTRODUCTION

In the past decade, metal-halide perovskite solar cells (PSCs) have experienced remarkable success, with their power conversion efficiency (PCE) increasing from only 3.8% in 2009 to more than 26% in 2025.[1] Moreover, their application as a front cell in a multijunction solar cell configuration with silicon and copper indium gallium (di)selenide (CIGS) has captured the attention of the photovoltaic (PV) community. Their unprecedented progress is a consequence of their unique properties such as bandgap tunability,[2] high absorption coefficient,[3] and long charge carrier diffusion lengths.[4] The current challenges of PSCs mainly lie in their limited stability[5] and upscaling the technology while retaining a similar PCE.[6] Both stability and scalability are of utmost importance toward the commercialization of this technology and are, therefore, the current area of focus for the PV community.

Besides the perovskite active layer, charge transport layers (CTLs) and the interfaces they form with the perovskite layer are imperative in deciding their performance as well as the long-term stability. Amidst diverse thin-film deposition techniques, the atomic-layer deposition (ALD) technique is one of the most appealing ones for the growth of CTLs.[7−9] Apart from its natural tendency to form pinhole-free and conformal films, ALD can potentially offer several benefits to further improve PSCs. Many ALD-grown materials such as TiO_2,[10] SnO_2,[11−13] and NiO[14,15] have been demonstrated by different research groups as electron and hole transport layers (ETLs and HTLs, respectively) in PSCs. These layers are mostly deposited before the perovskite layers in the n−i−p (TiO_2, SnO_2) and p−i−n (NiO) structures. However, reports on direct deposition of ALD-grown layers on top of perovskites are rather limited. Today, all the best performing tandem

Received: April 5, 2025
Revised: May 22, 2025
Accepted: May 23, 2025
Published: June 3, 2025

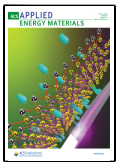

© 2025 The Authors. Published by American Chemical Society

configurations employ PSCs containing a combination of evaporated organic and ALD-grown inorganic ETLs.[16−21] Organic CTLs ([6,6]-phenyl-C61-butyric acid methyl ester, PCBM, and C_{60}) act as efficient electron extraction layers and protect the perovskite from the ALD process. At the same time, the inorganic layer (ALD SnO_x) shields the underlying structure against the subsequent transparent conductive oxide (TCO) sputter process in a semitransparent PSC. Furthermore, Brinkmann et al. demonstrated in their study that ALD SnO_x acts as an impermeable barrier against the inflow of moisture and outflow of perovskite decomposition products in p−i−n PSCs.[22] Consequently, it subdued the overall degradation of perovskites and improved the device stability.

Organic layers themselves have poor tolerance to mechanical, chemical, and thermal stresses. Moreover, the perovskite/C_{60} interface is a major contributor to nonradiative losses in a p−i−n PSC; thereby, an interlayer is required in between to further enhance the performance.[23] Omitting the use of organic layers may not only improve the stability but also make the structure more elegant as it would require fewer processing steps, thus potentially reducing the overall cost and complexity in device fabrication. Therefore, continuous efforts are being made to directly deposit inorganic layers by ALD on top of the perovskite absorbers. This approach has its own challenges, as the utilized ALD chemistries have usually proven harmful toward perovskites.

Hultqvist et al. investigated the interface between $Cs_{0.05}FA_{0.79}MA_{0.16}PbBr_{0.51}I_{2.49}$ and ALD SnO_x grown using tetrakis(dimethylamino)tin(IV) (TDMASn) and H_2O as precursors.[24] They reported the occurrence of a reaction between TDMASn and the perovskite surface, which leads to the formation of a performance-limiting interfacial layer. In addition, Bracesco et al. also studied the interfacial chemistry between $Cs_{0.15}FA_{0.85}Pb(I_{0.92}Br_{0.08})_3$ and ALD SnO_x and titanium oxide (TiO_x) by employing TDMASn and tetrakis-(dimethylamino)titanium(IV) (TDMATi) as metal precursors.[25] The undesired interface formation was mainly reported for the perovskite and SnO_x combination and was linked to the redox reaction happening between the Sn metal center and the halide moieties from the perovskite. However, they did not observe any redox reactions between the perovskite and TiO_x. Recently, Mallik and co-workers also studied the effect of ALD SnO_x deposition on $FA_{0.7}Cs_{0.3}Pb(I_{0.9}Br_{0.1})_3$ perovskite composition, toward the solar cell performance.[26] Their findings revealed the formation of new species and an upward band-bending at the interface between $FA_{0.7}Cs_{0.3}Pb(I_{0.9}Br_{0.1})_3$ and ALD SnO_x, ultimately acting as an electron extraction barrier and negatively affecting the solar cell performance. However, several research groups have successfully demonstrated the beneficial effects of depositing aluminum oxide (AlO_x) on top of perovskite toward the solar cell performance.[27−29] ALD AlO_x has been adopted as an interlayer in both n−i−p and p−i−n structures and has been identified to both passivate the surface of the perovskite and improve the stability of the device. In this scenario, the resulting interface between perovskite and AlO_x is likely favorable toward device performance.

The formed interface between perovskite and ALD metal oxides is highly sensitive to numerous factors such as perovskite composition, ALD deposition temperature, and ALD precursors. In the past studies, the perovskite/ALD metal-oxide interface has been mainly explored by utilizing mixed cation and mixed halide perovskite compositions. As discussed before, these studies usually comprised a combination of Cs^+, FA^+, and MA^+ cations and I^- and Br^- anions, making it challenging to understand how individual ions influence the formation of the interface. The choice of both A site cations and halides has been known to influence the phase stability, ion migration, surface interaction, and degradation of the perovskites and, consequently, the long-term stability of the solar cell.[30−32] The continuous rise toward the adoption and incorporation of FA^+ cation in the perovskites employed in all the top-efficiency single and multijunction solar cell structures[33,34] makes it crucial to understand how FA^+ interacts with the ALD SnO_x process. Therefore, we have specifically based our study on FA-only perovskite compositions, without incorporating additional cations at the A site. In particular, we have worked with simple perovskite compositions, which include $FAPbI_3$ and $FAPbBr_3$, which will help in untangling the contributions of both A site cation and halide ions toward the reaction with the ALD SnO_x process. We mainly focus on how FA^+ and halides (I^- and Br^-) play a part in defining the perovskite/ALD SnO_x interface. In order to systematically study the interface, we conducted soft and hard X-ray photoelectron spectroscopy (SOXPES and HAXPES) studies. In the SOXPES part, we prepared a series of $FAPbX_3$ (X: I and Br)/SnO_x samples with varying numbers of ALD cycles and studied the formation of the interface by recording spectra of relevant elements on each sample. The thickness of SnO_x that is utilized in a solar cell structure is significantly larger than the probing depth of soft X-rays. Thus, in order to gain in-depth and complementary knowledge of the solar cell representative interface between $FAPbX_3$ and ALD SnO_x, we performed HAXPES measurements in parallel.

EXPERIMENTAL DETAILS

Sample Fabrication. [4-(3,6-Dimethyl-9*H*-carbazol-9-yl)butyl]-phosphonic acid (Me-4PACz) was purchased from Dyenamo. Lead iodide (PbI_2, 99.99% trace metal basis) and lead bromide ($PbBr_2$, 99.99% trace metal basis) were obtained from TCI Chemicals. Formamidinium iodide (FAI, 99.99%) and formamidinium bromide (FABr, 99.99%) were provided by Greatcell Solar Materials. 2,2′,7,7′-Tetrakis[*N*,*N*-di(4-methoxyphenyl)amino]-9,9′-spirobifluorene (Spiro-OMeTAD) was obtained from Borun. Lithium bis-(trifluoromethanesulfonyl)imide (Li-TFSI), 4-*tert*-butylpyridine (TBP), dimethylformamide (DMF), methyl sulfoxide (DMSO), methanol, chlorobenzene, and acetonitrile were purchased from Sigma-Aldrich. [6,6]-Phenyl-C61-butyric acid methyl ester (PCBM) and poly(9,9-bis(3′-(*N*,*N*-dimethyl)-*N*-ethylammonium-propyl-2,7-fluorene)-*alt*-2,7-(9,9 dioctylfluorene))dibromide (PFN-Br) were acquired from Ossila. Tetrakis(dimethylamino)tin(IV) (TDMASn) was purchased from Pegasus Chemicals.

Transparent conductive oxide (TCO) substrates, indium tin oxide (ITO) and fluorine-doped tin oxide (FTO) substrates were cleaned thoroughly by sonicating for 30 min each in Hellmanex soap, deionized water, acetone, and ethanol. Cleaned substrates were dried using a nitrogen gun and then treated in a UV-ozone cleaner for 30 min. Following the treatment, samples were immediately transferred to a nitrogen-filled glovebox for the deposition of hole transport material. A 0.4 mg/mL Me-4PACz solution in methanol was mixed with 0.4 mg/mL PFN-Br solution in methanol (4:1 ratio) to improve perovskite wetting on top of a Me-4PACz monolayer.[35] The resulting solution was spin-coated on ITO at 4000 rpm for 30 s and then annealed for 10 min at 100 °C. Subsequent perovskite deposition was conducted in air (RH < 30%) as follows:

> $FAPbI_3$: 1.8 M $FAPbI_3$ solution containing 0.63 M MACl was prepared in 4:1 DMF and DMSO. The solution was spin-coated at 6000 rpm for 50 s, and diethyl ether antisolvent was

https://doi.org/10.1021/acsaem.5c00968
ACS Appl. Energy Mater. 2025, 8, 8467−8478

dispensed at 15 s from the start of the program. The films were annealed at 150 °C for 10 min to obtain α-$FAPbI_3$ perovskite.

$FAPbBr_3$: 1.1 M $PbBr_2$ solution was prepared in 9:1 DMF and DMSO. The solution was stirred overnight at room temperature and briefly heated at 70 °C before spin-coating. It was spin-coated using a two-step program, 1500 rpm for 30 s and 3000 rpm for 20 s, and immediately heated at 70 °C for 1 min. Afterward, 0.065 g/mL FABr solution in methanol was spin-coated at 2000 rpm for 30 s. Finally, samples were annealed at 150 °C for 25 min and $FAPbBr_3$ films were obtained.

For the interface studies, as-deposited perovskite samples were transferred into a microchemistry F120 ALD reactor. ALD SnO_x was grown using tetrakis(dimethylamino)tin(IV) (TDMASn) as the metal precursor and H_2O as the coreactant. A TDMASn bottle was preheated using a water bath at 40 °C. SnO_x was grown at 90 °C using the cycle sequence TDMASn/N_2 purge/H_2O/N_2 purge with pulse times of 0.4/0.8/0.4/0.8 s. The growth per cycle of the ALD SnO_x process was obtained by depositing it on a quartz substrate using X-ray reflectivity measurements, which corresponds to 0.124 nm/cycle. Thickness values obtained from transmission emission microscopy (TEM) for 250 cycles of ALD SnO_x on $FAPbI_3$ and $FAPbBr_3$ were in the range of 30−35 nm. It is important to note that the nucleation of the SnO_x process will be dependent on the substrate on which it is being grown, which may eventually influence the resulting thickness from the same number of ALD cycles on different substrates (including different perovskite compositions). The surface-inhibited growth of the ALD SnO_x process on perovskites has been discussed previously in detail.[24] All the prepared samples were briefly exposed to air during the transfer from the ALD reactor to the subsequent process or measurement setup.

Depending on the targeted p−i−n structure, the PCBM layer was incorporated between perovskite and ALD SnO_x. 20 mg/mL PCBM solution in chlorobenzene was spin-coated atop of perovskite at 2000 rpm for 30 s in a N_2-filled glovebox. In the end, 80 nm-thick Ag was deposited on top of the ALD SnO_x using thermal evaporation.

For the fabrication of the n−i−p structure, colloidal SnO_2 particles (Alfa Aesar) were diluted using H_2O in the ratio 1:4. The solution was spin-coated on UV−O_3-treated ITO (for $FAPbI_3$) or FTO (for $FAPbBr_3$) substrates at 3000 rpm for 30 s and annealed at 150 °C for 30 min. As the next step, these samples were treated in a UV−O_3 cleaner for 20 min and perovskite ($FAPbI_3$ or $FAPbBr_3$) was deposited using the methods described above. Spiro-OMeTAD was employed as the HTM in this structure. A 70 mM Spiro-OMeTAD solution was prepared by dissolving in chlorobenzene. Further, TBP, Li-TFSI (1.8 M in acetonitrile), and FK-209 (0.25 M in acetonitrile) were used as additives. The obtained solution was spin-coated at 4000 rpm for 30 s. Finally, 80 nm-thick Au was thermally evaporated to complete the structure.

Characterization Methods. X-ray diffraction measurements were performed using a Panalytical Empyrean instrument in grazing incidence mode. The setup comprised a focusing X-ray mirror on the incident beam's path and a d-core 0.27° parallel-plate collimator coupled with a PIXcel detector. All of the measurements were acquired at an incidence angle of 1° in the 2θ range of 3−50° with a step size of 0.03°.

Scanning electron microscopy micrographs were captured using a Zeiss LEO 1550 (or 1530) instrument using an in-lens detector. All of the samples were prepared by mounting aluminum tape to minimize surface charging. To mitigate the charging effects further, the value of electron high tension (EHT) was kept low at 4 kV and the beam's aperture size was kept small to a diameter of 10 μm.

Photoluminescence measurements were collected on a Cary Eclipse fluorescence spectrophotometer. The setup consisted of a xenon lamp coupled to a monochromator. The samples were scanned between 400 and 900 nm with a step size of 1 nm.

Current−voltage characteristics were attained using a Wave Laboratories SINUS-70 LED-based solar simulator. All the devices were measured under an illumination of 100 mW/cm^2, and the active area of the devices was defined using a black shadow mask of area 0.0688 cm^2. Data were recorded in the range from −0.2 to 1.5 V with a voltage increment of 0.02 V and a voltage settle time of 50 ms.

Soft X-ray photoelectron spectroscopy measurements were performed by using a PHI Quantera II scanning XPS microprobe with monochromatized Al Kα (1486.6 eV) and a beam diameter of 100 μm. In the present study, these measurements are referred to as SOXPES. The base pressure in the analysis chamber was about 1×10^{-9} mbar during the measurements. Electron and ion guns were used to provide charge neutralization. All the core levels were recorded using a pass energy of 55 eV and an energy step of 0.1 eV. The binding energy positions of the bare perovskite samples were calibrated with respect to the position of adventitious carbon (284.8 eV). All the remaining perovskite samples containing ALD SnO_x on top were then calibrated by aligning to the Pb $4f_{5/2}$ peak from their bare counterparts (set to 143.45 eV for $FAPbI_3$ and 143.31 eV for $FAPbBr_3$). Note that the position of a more intense Pb $4f_{7/2}$ peak coincides with the position of the Sn 4s peak; therefore, to simplify the analysis, we instead chose the Pb $4f_{5/2}$ peak in our studies. The spectra were fitted using the XPST program package on Igor Pro. The peaks were modeled using the mixed Gaussian−Lorentzian (pseudo-Voigt) function and by subtracting a Shirley background. The elemental ratios were calculated by using the integrated areas of the elements obtained from the fitted spectra. The Scofield photoionization cross section[36] and inelastic mean free path (IMFP) of each core level were also taken into account in these calculations. The utilized formula can be found in the Supporting Information.

Hard X-ray photoelectron spectroscopy (HAXPES) was performed at the I09 beamline at Diamond Light Source, U.K., using two different X-ray photon energies of 2.2 and 6.6 keV with pass energies of 100 and 200 eV, respectively. The survey scans were measured with a step size of 0.5 eV, the individual core levels and valence band spectra were recorded with a smaller step size of 0.1 eV, and the dwell time was fixed at 176 ms. High-intensity measurements on the perovskite samples showed X-ray damage for 6.6 keV photon energy, as expected. Therefore, to reduce the X-ray damage, we decreased the incident photon flux to the point where we collected spectra in which we did not observe any X-ray damage during the measurements. This process was done by measuring various core levels, Pb 4f, I 3d, and N 1s in a loop sequence. During the measurements, the base pressure of the main chamber was maintained at $\sim 10^{-10}$ mbar. The photoelectrons were detected using a VG Scienta EW4000 HAXPES with a 70 frame/s CCD camera. All the spectra were calibrated with respect to C 1s spectra by utilizing the actual binding energy value of the C−C bond at 284.8 eV. The spectra were analyzed using the same method as utilized for SOXPES measurements. The survey scans obtained using SOXPES and HAXPES measurements demonstrated all the expected peaks such as Pb, I/Br, N, C, O, and Sn, free from any additional elements.

RESULTS

Perovskite Characterization. $FAPbI_3$ and $FAPbBr_3$ perovskite films were initially evaluated in their well-established n−i−p structures, as shown in Figure S1. XRD patterns and SEM images confirm the formation of the targeted phase-pure perovskite compositions with large grain sizes. Moreover, both perovskite compositions resulted in satisfactory top PCEs of 20.2% and 7.1% for $FAPbI_3$ and $FAPbBr_3$ PSCs, respectively. After optimizing perovskite films in n−i−p structures, we subsequently fabricated the p−i−n structures shown in Figure 1a, to study the compatibility of ALD SnO_x with $FAPbI_3$ and $FAPbBr_3$. Here, SAM (Me-4PACz:PFN-Br) was used as the HTL and ALD SnO_x as the ETL. Before fabricating these structures, the quality of the two perovskites on SAM was examined thoroughly using XRD, SEM, and PL (shown in Figure S2). XRD diffractograms of these samples (presented in Figure S2a) matched well with the previously reported XRD patterns of $FAPbI_3$[37] and $FAPbBr_3$.[38]

https://doi.org/10.1021/acsaem.5c00968
ACS Appl. Energy Mater. 2025, 8, 8467−8478

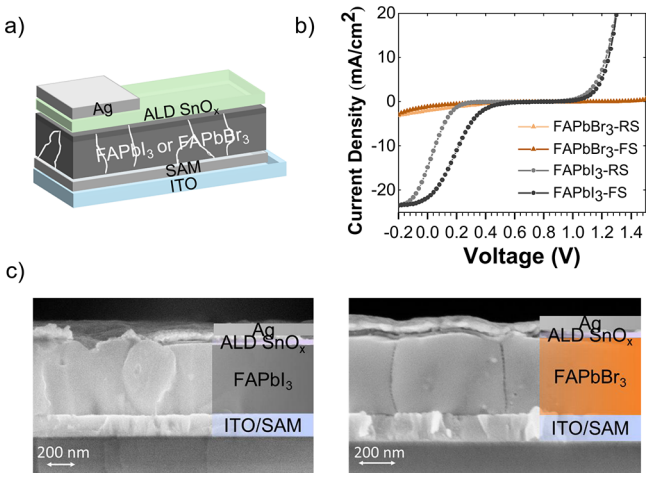

Figure 1. (a) Fabricated p−i−n PSC structure, utilizing either $FAPbI_3$ or $FAPbBr_3$ as the absorber. (b) Measured reverse scan (RS) and forward scan (FS) current−voltage characteristics and (c) SEM cross-sectional images of the PSC shown in (a).

The obtained patterns confirm the formation of cubic perovskite crystal structures. In the case of $FAPbI_3$, the presence of a strong reflection at a 2θ of ∼14° confirms the formation of the photoactive α-phase. Concurrently, no peak corresponding to the δ-phase (2θ = 11.8°) was observed, thus confirming the formation of phase-pure $FAPbI_3$. Furthermore, SEM micrographs indicate the formation of uniform and compact films without the presence of any major pinholes. Finally, photoluminescence spectra shown in Figure S2c demonstrate the emission peaks for $FAPbI_3$ and $FAPbBr_3$ at wavelengths of 807 nm (1.53 eV) and 551 nm (2.25 eV), respectively. Both the values match well with the already reported values in the literature.[39−41]

Solar Cell Characteristics. The measured current density−voltage ($J-V$) characteristics from the $FAPbI_3$ and $FAPbBr_3$ p−i−n solar cell structures are demonstrated in Figure 1b. In both p−i−n structures, the obtained $J-V$ curves have an s-shape with significantly low values of the fill factor (FF). Such characteristics are typically observed due to the presence of an energetic barrier at the absorber/transport layer interface and have also been previously reported in organic and perovskite solar cells.[42,43] Such an issue is mainly observed on depositing ALD SnO_x directly on top of the two perovskites. Figure S3 shows the $J-V$ characteristics of the same p−i−n structures but with the PCBM organic layer in between ALD SnO_x and perovskites. With an extra PCBM layer, the devices show a much higher FF, confirming that the problem is at the ALD SnO_x/perovskite interface. Similar $J-V$ curves have also been previously observed for the direct deposition of ALD SnO_x on top of perovskites with different compositions; there, the interface was considered to be the main problem.[24,25] The SEM cross sections of the $FAPbI_3$ (left) and $FAPbBr_3$ (right) p−i−n structures are shown in Figure 1c. From the micrographs, it can be interpreted that the bulk of the perovskite is not noticeably affected by ALD SnO_x deposition, as the layer remains compact with defined grains.

XRD Results. To further confirm that the bulk of the perovskites is not impacted following SnO_x deposition, we carried out XRD measurements on $FAPbI_3$/ALD SnO_x and $FAPbBr_3$/ALD SnO_x samples (presented in Figure 2). As expected, no additional peaks were observed from ALD SnO_x due to its amorphous nature. Moreover, the minimal value of film's thickness will have a minute contribution to the overall diffraction volume. From the XRD pattern, it can be observed that the general crystal structures of both perovskites are unharmed. Figures 2b and 2c, respectively, indicate the (100) reflections for the $FAPbI_3$ and $FAPbBr_3$ samples before and after SnO_x deposition. There are no recognizable changes in the full width at half-maximum (fwhm) values of the perovskite

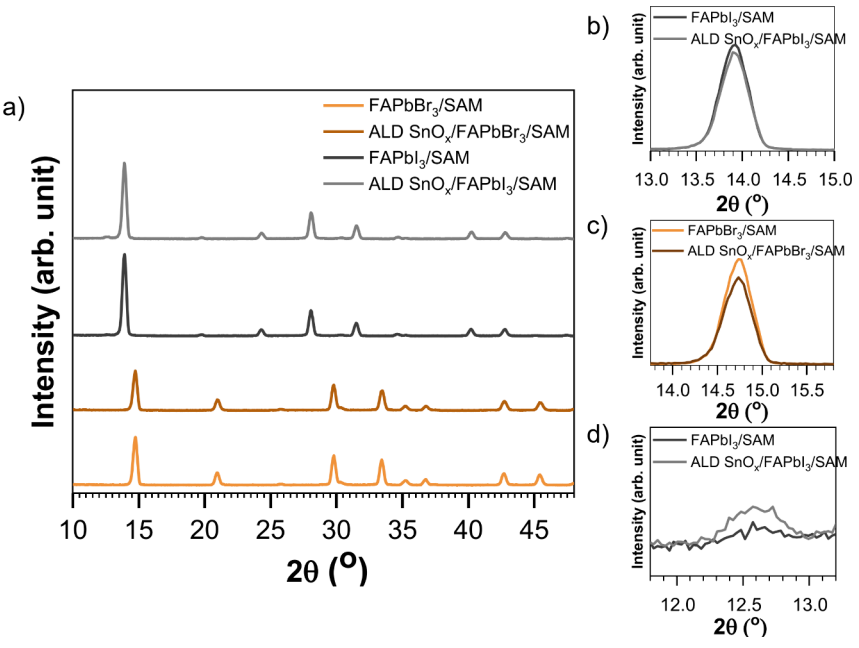

Figure 2. (a) X-ray diffraction pattern recorded on $FAPbI_3$ and $FAPbBr_3$ films with and without ALD SnO_x films deposited on top. (b, c) Comparison between (100) peaks obtained from bare $FAPbX_3$ (X: I and Br) samples and with SnO_x on top. (d) XRD region showing the existence of PbI_2 peak post SnO_x deposition on $FAPbI_3$.

https://doi.org/10.1021/acsaem.5c00968
ACS Appl. Energy Mater. 2025, 8, 8467−8478

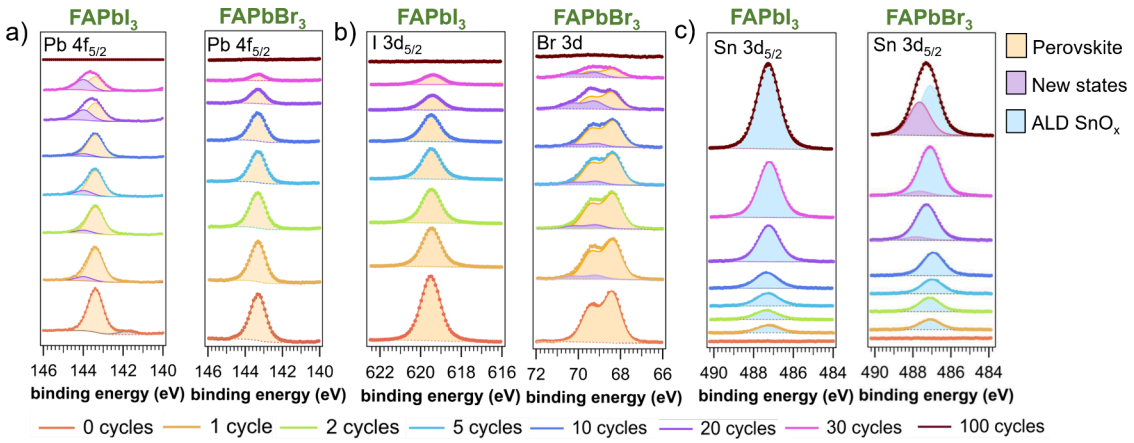

Figure 3. Comparison between the XPS spectra of (a) Pb $4f_{5/2}$ and (b) halides (I $3d_{5/2}$ and Br 3d) and (c) Sn $3d_{5/2}$ core levels obtained from $FAPbI_3$/ALD SnO_x (left) and $FAPbBr_3$/ALD SnO_x (right) samples with different numbers of ALD cycles.

(100) reflection post SnO_x deposition (Figure S4). Thereby, this confirmed that the bulk crystal structure remains undistorted for both perovskites, $FAPbI_3$ and $FAPbBr_3$, subsequent to the SnO_x layer deposition. However, in the case of the $FAPbI_3$ sample, we observed an emergence (or increase) of a reflection in the ALD SnO_x/$FAPbI_3$ sample around a 2θ of ∼12.6 (indicated in Figure 2d), which is usually assigned to PbI_2 matched with the ICDD database (ICDD 04-014-2519), thus indicating the likelihood of a reaction between $FAPbI_3$ and SnO_x resulting in the formation of PbI_2. To further investigate the reaction chemistries between $FAPbX_3$ perovskites and ALD SnO_x, in particular, the formation of the interface between the two layers, we have employed SOXPES and HAXPES, which are discussed in the next sections.

Interface Study Using X-ray Photoelectron Spectroscopy. *Analysis Using SOXPES.* The stability of $FAPbI_3$ and $FAPbBr_3$ was first evaluated under an X-ray beam as a function of time. Two sets of measurements were performed in a sequential fashion at a specific spot on the sample, where it took approximately 40 min to record each set of core levels. These measurements are presented in Figure S5. The two measurements resulted in spectra with only minor differences that do not affect the trends observed in our investigations, thus confirming the stability of the employed perovskites within the time frame of measurements. To study the interface between $FAPbX_3$ and ALD SnO_x, a series of $FAPbX_3$ samples containing different numbers of ALD cycles of SnO_x were prepared. In particular, 1, 2, 5, 10, 20, 30, and 100 ALD cycles of SnO_x were deposited on individual $FAPbX_3$ samples, and the XPS spectra of relevant core levels were measured on each sample. By this, we investigate how the chemistry develops for $FAPbI_3$ and $FAPbBr_3$ at the interface with SnO_x as we subsequently grow thicker and thicker SnO_x on the perovskites; thereby, we are able to investigate the perovskites, the interface, and the SnO_x and above as the layer evolves.

The recorded spectra for Pb 4f, I 3d, and Sn 3d cores levels for $FAPbI_3$ samples and for Pb 4f, Br 3d, and Sn 3d cores levels for $FAPbBr_3$ are presented in Figure S6, and the corresponding fitted spectra of these plots are shown in Figure 3. The parameters obtained from fitting these spectra can be found in Tables S1 and S2. Here, different samples are labeled depending on the number of ALD cycles that were grown on top of the two perovskites. For example, 0 cycle corresponds to bare perovskites without any SnO_x coating on top and 100 cycles correspond to samples containing 100 ALD cycles of SnO_x on perovskites. For both, $FAPbI_3$ and $FAPbBr_3$, it can be observed that the intensities of Pb 4f, I 3d, and Br 3d core-level lines from the perovskites decrease as we increase the thickness (number of cycles) of ALD SnO_x, while the intensity of the Sn 3d core-level line increases. There is a significant broadening in the Pb 4f peak for $FAPbI_3$ samples as we increase the number of ALD cycles, while such effects are not evident in the case of $FAPbBr_3$ samples. Conversely, Sn 3d peaks demonstrate slight broadening for $FAPbBr_3$ samples but not for $FAPbI_3$ samples (normalized spectra are shown in Figure S7). Furthermore, we can clearly observe a broadening of the Br 3d core-level peaks along with subsiding intensities after SnO_x deposition, whereas I 3d core-level peaks do not exhibit any such widening. Interestingly, we could even detect the presence of a Br 3d peak in the $FAPbBr_3$ sample containing 100 cycles of ALD SnO_x, while no I 3d signal could be observed in the $FAPbI_3$ sample with 100 cycles of ALD SnO_x (presented in Figure S8).

Note that the $FAPbI_3$ sample without SnO_x coating showed the presence of a Pb^0 peak at 141.62 eV in addition to the main peak corresponding to Pb in perovskite at 143.45 eV. Since no changes in the core levels were observed as a function of time under X-ray illumination (Figure S5), Pb^0 is likely present on the perovskite surface before the XPS measurements. In the case of $FAPbI_3$/ALD SnO_x samples, there is an emergence of a new peak in Pb $4f_{5/2}$ core-level spectra, indicated in purple, and shifted by 0.6 eV with respect to Pb in $FAPbI_3$, while the I 3d core-level spectra did not reveal any noticeable changes in its fwhm values. These observations indicate the formation of PbI_2, as the Pb−I in PbI_2 has previously been reported to have a similar binding energy difference in the Pb 4f core level with respect to Pb−I in $FAPbI_3$.[44,45] In addition, the presence of PbI_2 in the XRD pattern of the ALD SnO_x/$FAPbI_3$ sample (Figure 2d) is consistent with the association of the new peak in Pb $4f_{5/2}$ core-level spectra to Pb−I in PbI_2. Aside from this, there was no increase in the fwhm of Sn 3d core-level peaks following SnO_x deposition (normalized Sn 3d spectra for all of the samples are shown in Figure S7a). Concerning $FAPbBr_3$/ALD SnO_x, we mainly observed modifications in the peak shape/fwhm of Br 3d and Sn 3d core levels after SnO_x deposition, whereas no new peak was observed in the Pb 4f core-level spectra, which was the case in $FAPbI_3$/ALD SnO_x

https://doi.org/10.1021/acsaem.5c00968
ACS Appl. Energy Mater. 2025, 8, 8467−8478

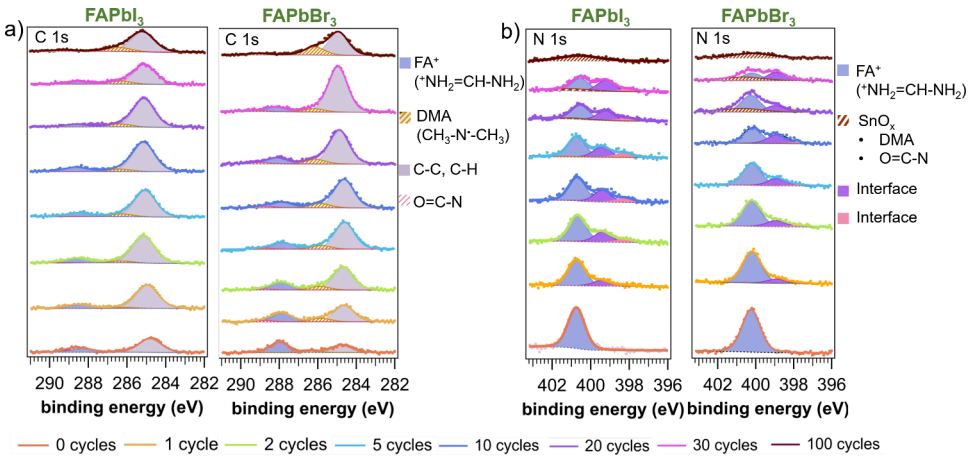

Figure 4. XPS spectra of (a) C 1s and (b) N 1s core levels obtained using an Al Kα X-ray source for $FAPbI_3$/ALD SnO_x (left) and $FAPbBr_3$/ALD SnO_x (right) samples.

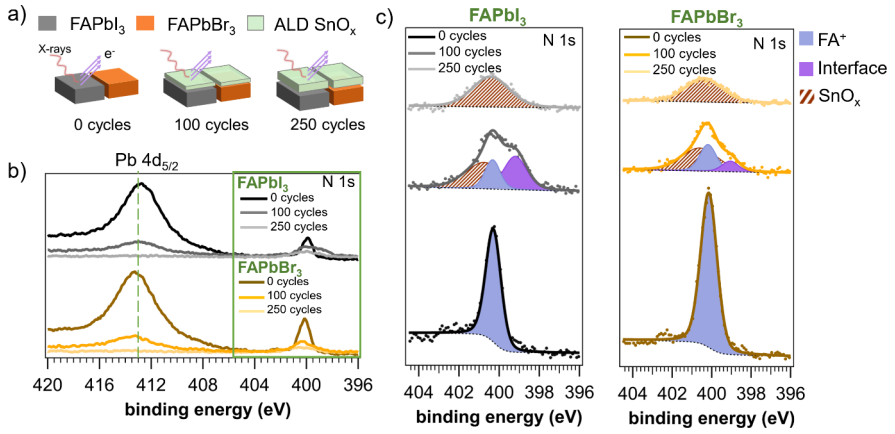

Figure 5. (a) Schematic showing the method adopted to probe the interface between $FAPbX_3$ and ALD SnO_x using HAXPES. (b) N 1s core-level spectra measured for $FAPbX_3$ without any ALD SnO_x and with 100 and 250 ALD cycles of SnO_x using a 6.6 keV X-ray energy source. (c) Fitted spectra of these samples measured using a 6.6 keV X-ray energy source.

samples. This implies modification of the chemical surroundings around Br and Sn elements.

O 1s, C 1s, and N 1s core-level spectra obtained for the two perovskite samples containing different numbers of ALD cycles are shown in Figure S9, and the reference spectra recorded for ALD SnO_x films on soda-lime glass (SLG) are shown in Figure S10. O 1s core-level spectra comprise Sn−O and Sn−OH/−C═O contributions.[46] The detailed discussion on the core-level spectra of the O 1s can be found in the Supporting Information. C 1s and N 1s spectra, shown in Figure S9b,c, provide information about formamidinium ion (FA^+). In addition, ALD SnO_x coating also has contributions in N 1s and C 1s spectra, originating from the Sn precursor, tetrakis-(dimethylamino)tin(IV) (TDMASn) (Figure S10). This is mainly due to the incomplete ligand exchange between −DMA and −OH and the ligand's desorption especially at low temperatures.[47,48] In order to consider all the contributions and differentiate between perovskite, SnO_x, and the changes in the interfacial environment, N 1s and C 1s were fitted accordingly; the details are presented in Tables S3 and S4. The fitted XPS spectra of C 1s are shown in Figure 4a, the blue peak corresponds to FA^+ from the perovskites, and the peak with a brown pattern is linked to the dimethylamine (DMA) ligand of the Sn precursor. In addition, the peak in gray corresponds to C−C and C−H bonds, whereas a small contribution represented with a pink pattern likely relates to N−C═O, as it has previously been discussed to form during the ALD of SnO_x.[46] These contributions are also indicated alongside the figure. Figure 4b presents the N 1s spectra and depicts the involvements of different chemical bonds associated with nitrogen, which include FA^+ (blue) originating from the perovskites, nitrogen contributions from SnO_x (maroon pattern), and new interfacial states (pink and purple). The broad peak assigned to SnO_x in N 1s spectra is a combination of contributions from the DMA ligand and N−C═O, and the two contributions are likely not well-separated in N 1s spectra as they are in C 1s spectra. From the fitted C 1s and N 1s core-level spectra, it is evident that the signal from FA^+ decreases as the number of ALD cycles increases. Similarly, as the thickness of SnO_x increases, the contribution of the corresponding metal ligand (DMA) becomes larger in both the C 1s and N 1s core-level spectra. In addition, interestingly, we detect the formation of new chemical states at the interface in N 1s core-level spectra (purple and pink, at lower binding energies).

Fitted core-level spectra for Pb $4f_{5/2}$, I $3d_{5/2}$, Sn $3d_{5/2}$, and N 1s for $FAPbI_3$/ALD SnO_x samples and Pb $4f_{5/2}$, Br $3d_{5/2}$, Sn $3d_{5/2}$, and N 1s for $FAPbBr_3$/ALD SnO_x were utilized to calculate the elemental ratios for samples containing different numbers of ALD cycles. The obtained values of the ratios X/

https://doi.org/10.1021/acsaem.5c00968
ACS Appl. Energy Mater. 2025, 8, 8467−8478

Pb (X: I and Br), N/Pb, and Sn/Pb for the two sample sets were calculated using eq S1 and are given in Table S5 and represented in Figure S11. The ratio between I and Pb decreases from 2.6 for bare $FAPbI_3$ to ~2 for $FAPbI_3$ samples containing 1, 2, 5, and 10 cycles and below 1 for 20 and 30 cycles of ALD SnO_x. The calculated ratio between Br and Pb for bare $FAPbBr_3$ is 2.7 and stays around the same value as we grow 1, 2, 5, and 10 cycles of SnO_x and finally increases as a function of ALD cycles of SnO_x. As expected, the ratio between Sn and Pb increases as we grow SnO_x on both $FAPbI_3$ and $FAPbBr_3$. However, the value of this ratio is higher in the case of $FAPbBr_3$ for the same number of ALD cycles, indicating that ALD SnO_x nucleates differently on $FAPbBr_3$ and $FAPbI_3$. Similarly, the N/Pb ratio also increases for both perovskites due to additional N contributions from SnO_x as it grows, mainly following 20 and 30 ALD cycles of SnO_x. This increase is more prominent in the case of $FAPbBr_3$ as was also observed in the corresponding Sn/Pb ratio. In addition, the relative ratios of different nitrogen contributions are also presented in Figure S11c, which demonstrates that the contribution from FA^+ decreases while contributions from the interfacial states increase in the case of both perovskites as the number of ALD cycles increases.

Analysis Using HAXPES. To further understand and confirm the existence of new nitrogen and carbon states at the interface, we carried out HAXPES measurements of the buried perovskite/SnO_x interface. Similar to the case of SOXPES, N 1s and C 1s core-level spectra were recorded at a spot on the sample as a function of time to check their stability under X-rays (presented in Figure S12). No noticeable changes were observed between the two measurements, thus confirming their stability during the period of the measurements. Here, we analyze three samples for both perovskites: $FAPbX_3$ (X: I and Br) without SnO_x and with 100 and 250 ALD cycles of SnO_x. The schematic representation of the measurements performed is elucidated in Figure 5a, where the HAXPES measurements were performed at 6.6 and 2.2 keV.

The results obtained for the N 1s core level for the two sample sets are shown in Figure 5b, $FAPbI_3$ (top) and $FAPbBr_3$ (bottom). The spectra were recorded over a wide range and also contain a signal from the Pb $4d_{5/2}$ core level at a value of around 413 eV. It is mainly the region between 398 and 403 eV that corresponds to the signal from the N 1s core level (indicated in the green box). The samples with 250 ALD cycles do not contain information from either the perovskite's bulk or from its interface with SnO_x since the Pb $4d_{5/2}$ peak intensity is too small to observe. Figure 5c shows the N 1s core-level spectra in more detail, and the fitting parameters are provided in Tables S6 and S7. The peak filled with a maroon pattern is potentially originating from the SnO_x layer due to the presence of nitrogen contributions discussed for the SOXPES measurements. To further confirm this, we also compared the N 1s spectra for $FAPbX_3$ with 250 ALD cycles of SnO_x to the ALD SnO_x reference deposited on soda-lime glass (SLG); normalized spectra for the same are shown in Figure S13c. All three samples show peaks with similar fwhm, thus supporting the assignment of the above-mentioned peaks. The HAXPES measurements for the perovskite samples with 100 ALD cycles of SnO_x give insights on the interfacial chemistry as we can observe a considerably intense Pb $4d_{5/2}$ peak from the perovskites. The fitted spectra for the two series are shown in Figure 5c. First, the N 1s core-level spectra for the bare perovskite samples and those with 250 ALD cycles of SnO_x were fitted individually. The obtained values of the parameters were then utilized and incorporated into the fitting profile of the perovskite samples with 100 cycles of SnO_x. The evident broadening in the N 1s peak for these samples implies the presence of additional nitrogen states (purple, at lower binding energy) beyond those from $FAPbX_3$ (X: I and Br) and SnO_x. This aligns well with the observations from the SOXPES part (Figure 4b).

The obtained C 1s core-level spectra are presented in Figure S14 for $FAPbI_3$ and $FAPbBr_3$ samples, and the fitted spectra are shown in Figure 6. The bare $FAPbX_3$ samples (0 cycles)

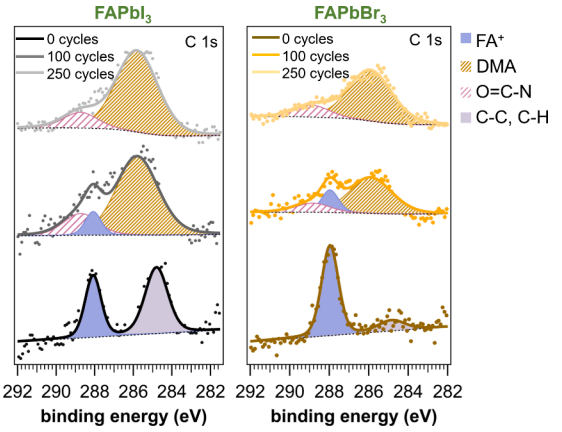

Figure 6. HAXPES C 1s core-level spectra measured for $FAPbX_3$ without any ALD SnO_x and with 100 and 250 ALD cycles of SnO_x using a 6.6 keV X-ray energy source.

consist of contributions from FA^+ and adventitious carbon (C−C and C−H). Similar to the case of N 1s spectra, the perovskites containing 250 cycles of ALD SnO_x provide information from the bulk of SnO_x, where it represents the presence of N−C═O at the highest binding energy value (pink pattern) as well as corresponds to the presence of the DMA ligand (brown pattern). Meanwhile, the ones with 100 cycles contain the information from the $FAPbX_3$/ALD SnO_x interface. The spectra were fitted in the same manner as the N 1s spectra (Figure 5); contributions from the bulk of perovskite and SnO_x were accounted for by separately fitting the C 1s spectrum of $FAPbX_3$ (0 cycle) and the ones with 250 cycles of ALD SnO_x on top. As-acquired fitting parameters from the bulk compositions were utilized in fitting the C 1s spectra of $FAPbX_3$/ALD SnO_x with 100 cycles. The samples with 100 cycles comprise the carbon contributions observed in ALD SnO_x as well as additional FA^+ peak from the perovskites, while no other distinct peak associated with the additional interfacial states could be identified. This corroborates the observations made in the SOXPES studies on the C 1s core level (Figure 4a).

DISCUSSION

X-ray photoelectron spectroscopy analysis conducted using different photon energies to study the implication of the direct deposition of ALD SnO_x on top of $FAPbX_3$ (X: I and Br) provides insights concerning the formation of new chemical environments at the interface. The results obtained from both soft and hard X-ray photoemission spectroscopy (SOXPES and HAXPES) measurements demonstrate the emergence of new peaks in the N 1s core level, related to the chemical changes occurring at the perovskite/SnO_x interface. In a former study

https://doi.org/10.1021/acsaem.5c00968
ACS Appl. Energy Mater. 2025, 8, 8467−8478

conducted by Palmstrom et al., degradation due to the interaction between $FA_{0.83}Cs_{0.17}Pb(I_{0.83}Br_{0.17})_3$ perovskite and TDMASn when growing SnO_x on top of perovskite was observed, especially at a higher deposition temperatures (150 °C).[49] They proposed exchange of the dimethylamine ligand from the TDMASn precursor with FA^+ as the most probable reaction pathway, which then leads to the removal of FA^+ from perovskite's lattice. Juarez-Perez et al. studied the thermal degradation of $FAPbX_3$ using coupled thermogravimetry−mass spectrometry analysis, where they observed a temperature-dependent decomposition of formamidinium.[50] In their study, they concluded that at temperatures below 100 °C, formation of formamidine and HCN products takes place in parallel. On the contrary, the temperatures above 95 °C lead to the formation of *sym*-triazine in their studies. Another study conducted by Bracesco et al. utilized $Cs_{0.15}FA_{0.85}Pb(I_{0.92}Br_{0.08})_3$ perovskite for in situ infrared spectroscopy and reported the deprotonation of formamidinium into formamidine and release of HX under prolonged heating at 100 °C in vacuum.[51] In addition, they also reported the deprotonation of formamidinium to occur and the formation of the *sym*-triazine byproduct to take place on exposing the TDMASn precursor to the perovskite. When inspecting our results, N 1s spectra obtained using SOXPES and HAXPES for both $FAPbI_3$ and $FAPbBr_3$ samples with ALD SnO_x on top show the emergence of new states occurring at binding energy values of around ∼399 eV (purple, Figures 4b and 5c). Compared to the information from the references, the emergence of this peak likely indicates the deprotonation of formamidinium into formamidine. Additionally, another peak observed in N 1s spectra at ∼398.5 eV (pink, Figure 4b) might be linked to the presence of triazine rings (N−C═N),[52] which possibly gets formed following the decomposition of FA^+ during the ALD process.[51]

Now, delving to the main part of the XPS study, i.e., understanding the role of halides (I and Br) employed in perovskites toward the formation of the interface with ALD SnO_x, Pb 4f spectra of the utilized $FAPbI_3$/ALD SnO_x samples clearly demonstrated the formation of PbI_2 at the interface, complimented by the XRD pattern, which showed an extra peak originating from PbI_2. Also, the calculated ratio between I and Pb was found to be ∼2 post 1, 2, 5, and 10 cycles of ALD SnO_x, indicating the formation of a PbI_2 chemical environment. However, strangely, this ratio dropped below 1 for samples containing 20 and 30 cycles of SnO_x. We speculate that there might be formation of Pb−O bonds, which decreases the corresponding ratio between I and Pb. In addition, in $FAPbI_3$/ALD SnO_x samples, no new chemical states of Sn were identified in Sn 3d core-level spectra. As illustrated in Figure 7, the combination of FA^+ decomposition and PbI_2 evolution contributes to the formation of a nonideal interface between $FAPbI_3$ and ALD SnO_x.

PbI_2, in particular has a wide bandgap[53] and can obstruct the transport of the generated charge carriers through the interface; consequently, these charge carriers would start to recombine at this interface, which would then eventually worsen the performance of the solar cell.[54] Furthermore, we have also observed the adverse effects of this interface on the stability of $FAPbI_3$ (shown in Figure S15a). The XRD pattern of the aged $FAPbI_3$ sample containing ALD SnO_x on top witnesses a decrease in the intensity of the photoactive α-$FAPbI_3$ and, at the same time, an emergence of another peak at ∼11.8°, compared to the bare $FAPbI_3$ sample. This new peak is known to be associated with the undesired wide-bandgap δ-

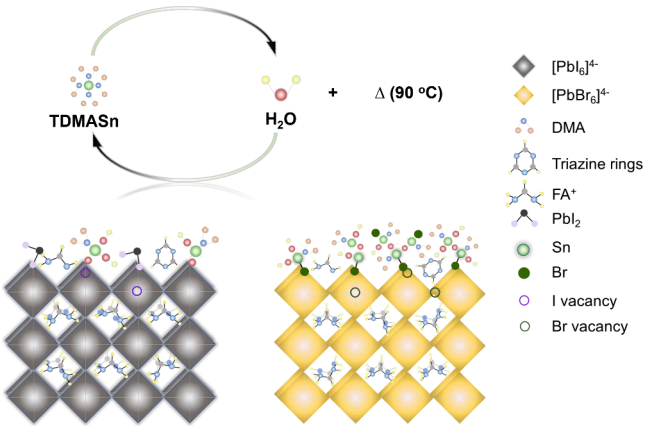

Figure 7. Illustration of the interfacial region formed as a result of the ALD SnO_x deposition on $FAPbI_3$ (left) and $FAPbBr_3$ (right).

$FAPbI_3$ phase.[37,55,56] This phase transition from α-$FAPbI_3$ to δ-$FAPbI_3$ could possibly happen due to the creation of defects post SnO_x deposition, which have been reported to lower the activation barrier from α-$FAPbI_3$ to δ-$FAPbI_3$.[57]

Interestingly, $FAPbBr_3$/ALD SnO_x exhibited a different interfacial chemistry compared to the $FAPbI_3$ counterparts. There was no indication toward the formation of $PbBr_2$ post SnO_x deposition on $FAPbBr_3$ since we did not observe any new chemical environments in the Pb 4f peak as well as no new peak corresponding to $PbBr_2$ was identified in the XRD pattern of these samples. However, we witnessed the emergence of new chemical states linked to Br and Sn, as evident from Br 3d and Sn 3d core-level spectra, similar observations have formerly been reported by Hultqvist et al.[24] These observations strongly point toward the interaction between Sn and Br, leading to the formation of Sn−Br bonds. At the same time, the presence of Br could be detected in the bulk of the ALD SnO_x. Moreover, the ratio between Br and Sn was found to eventually increase as ALD SnO_x grows, further confirming the migration of Br into the SnO_x layer. The formation of Sn−Br bonds and incorporation of Br in the matrix of SnO_x will modify its electronic properties. As a result, the transport of the charge carriers through the interface between $FAPbBr_3$ and ALD SnO_x or through Br-modified SnO_x could get impeded, thus adversely influencing the device performance. The apparent reaction between the tin metal center in TDMASn and bromine in perovskites, which leads to the diffusion of Br^- into the SnO_x matrix, may be difficult to avoid as it may still persist even after changing the tin precursor. Whether the interface formation between $FAPbX_3$ (X: I and Br) and ALD SnO_x starts with the deprotonation of FA^+ or the formation of PbI_2 ($FAPbI_3$) or Sn−Br products ($FAPbBr_3$) is not known.

Nevertheless, in both situations, i.e., $FAPbI_3$/ALD SnO_x and $FAPbBr_3$/ALD SnO_x, it is clear that a complex interfacial layer different from the two main components gets formed (presented in Figure 7). The formed interfacial layer potentially acts as an energetic barrier for the transport of the generated charge carriers, ultimately acting detrimental toward the solar cell performance. Thus, the choice of metal precursor is extremely crucial in ensuring the formation of a favorable interface with the perovskites, making it essential to find alternatives to ALD SnO_x for direct deposition atop of perovskites.

https://doi.org/10.1021/acsaem.5c00968
ACS Appl. Energy Mater. 2025, 8, 8467−8478

CONCLUSIONS

In order to understand previously reported surface reactions for the direct deposition of ALD SnO_x on top of complex perovskite materials, we investigated the growth of the ALD SnO_x transport layer directly on top of simple FA-based perovskites ($FAPbI_3$ and $FAPbBr_3$) in a p−i−n solar cell structure. The direct deposition of SnO_x on top of these perovskites resulted in poor device performance, while the use of a PCBM interlayer between the two dramatically improved the solar cells. Clearly, the bulk of both perovskites ($FAPbI_3$ and $FAPbBr_3$) remains intact post SnO_x deposition as evident from XRD diffractograms and SEM cross sections. It is mainly the interface between SnO_x and $FAPbX_3$ (X: I and Br) that negatively affects the resulting performance of the solar cells.

X-ray photoelectron spectroscopy studies on simple perovskite compositions using varying X-ray energies unveiled a detailed understanding on the involvement of different elements in forming new states at the interface. Decomposition of the FA^+ cation is witnessed as we grow SnO_x on $FAPbX_3$, irrespective of the employed halides. We hypothesize that FA^+ decomposition leads to its deprotonation and the formation of triazine species at the interface. Moreover, we found different interfacial chemistries involving iodine and bromine for the two samples, i.e., $FAPbI_3/SnO_x$ and $FAPbBr_3/SnO_x$, respectively, where the origin of these surface reactions would be difficult to discriminate for mixed halide perovskites. Deposition of SnO_x on $FAPbI_3$ leads to the formation of PbI_2 at the interface. Meanwhile, the interface between $FAPbBr_3$ and ALD SnO_x showed the existence of new Sn and Br states. Both of these formed interfaces act as transport barriers for the generated charge carriers and deteriorate the performance of the solar cells. This study provides insights into the different surface reactions and the compatibility between $FAPbX_3$ (X: I and Br) and the ALD process of SnO_x employing TDMASn and H_2O as the precursors, thus paving the way forward in designing suitable ALD processes or interlayers that would lead to high-quality interfaces with perovskite materials.

ASSOCIATED CONTENT

Supporting Information

The Supporting Information is available free of charge at https://pubs.acs.org/doi/10.1021/acsaem.5c00968.

XRD, SEM, PL, and $J-V$ characterization of $FAPbI_3$ and $FAPbBr_3$ solar cells; SOXPES and HAXPES results for $FAPbI_3$- and $FAPbBr_3$-related core levels for stability under X-rays; core-level spectra for $FAPbI_3$/ALD SnO_x and $FAPbBr_3$/ALD SnO_x samples measured using SOXPES and HAXPES, with tabulated details on the peak positions and fwhm values; XPS spectra of ALD SnO_x films on SLG; details on O 1s spectra obtained on $FAPbX_3$ (X: I and Br)/ALD SnO_x; elemental ratios obtained using SOXPES and details of the calculations; XRD patterns of fresh and aged $FAPbX_3$/ALD SnO_x (PDF)

AUTHOR INFORMATION

Corresponding Author

Bhavya Rakheja − *Department of Materials Science and Engineering; Solar Cell Technology, Uppsala University, Uppsala SE-751 03, Sweden;* orcid.org/0009-0000-8411-124X; Email: bhavya.rakheja@angstrom.uu.se

Authors

Adam Hultqvist − *Department of Materials Science and Engineering; Solar Cell Technology, Uppsala University, Uppsala SE-751 03, Sweden;* orcid.org/0000-0002-2402-5427

Rahul Mahavir Varma − *Department of Physics and Astronomy; X-ray Photon Science, Uppsala University, Uppsala SE-751 20, Sweden*

Natalia M. Martin − *Department of Materials Science and Engineering; Solar Cell Technology, Uppsala University, Uppsala SE-751 03, Sweden;* orcid.org/0000-0002-6881-4989

Karen Radetzky − *Department of Physics and Astronomy; X-ray Photon Science, Uppsala University, Uppsala SE-751 20, Sweden; Wallenberg Initiative Materials Science for Sustainability, Department of Physics and Astronomy, Uppsala University, Uppsala 751 20, Sweden;* orcid.org/0009-0007-0221-890X

Stefania Riva − *Department of Physics and Astronomy; X-ray Photon Science, Uppsala University, Uppsala SE-751 20, Sweden;* orcid.org/0000-0001-8449-1166

Evelyn Johannesson − *Department of Physics and Astronomy; X-ray Photon Science, Uppsala University, Uppsala SE-751 20, Sweden; Wallenberg Initiative Materials Science for Sustainability, Department of Physics and Astronomy, Uppsala University, Uppsala 751 20, Sweden*

Ute B. Cappel − *Department of Physics and Astronomy; X-ray Photon Science, Uppsala University, Uppsala SE-751 20, Sweden; Wallenberg Initiative Materials Science for Sustainability, Department of Physics and Astronomy, Uppsala University, Uppsala 751 20, Sweden;* orcid.org/0000-0002-9432-3112

Håkan Rensmo − *Department of Physics and Astronomy; X-ray Photon Science, Uppsala University, Uppsala SE-751 20, Sweden; Wallenberg Initiative Materials Science for Sustainability, Department of Physics and Astronomy, Uppsala University, Uppsala 751 20, Sweden;* orcid.org/0000-0001-5949-0997

Erik M. J. Johansson − *Department of Chemistry-Ångström Laboratory; Physical Chemistry, Uppsala University, Uppsala SE-751 20, Sweden;* orcid.org/0000-0001-9358-8277

Tobias Törndahl − *Department of Materials Science and Engineering; Solar Cell Technology, Uppsala University, Uppsala SE-751 03, Sweden;* orcid.org/0000-0001-7757-5847

Complete contact information is available at: https://pubs.acs.org/10.1021/acsaem.5c00968

Author Contributions

All authors have given approval to the final version of the manuscript.

Notes

The authors declare no competing financial interest.

ACKNOWLEDGMENTS

We acknowledge funding from the Solar Electricity Research Center, Sweden (SOLVE). SOLVE is cofinanced by the Swedish Energy Agency (project number 52693-1) as a national center of excellence. This work was partially supported by the Trygger Foundation, the STEM grant P50626-1, and the Wallenberg Initiative Materials Science

for Sustainability (WISE) funded by the Knut and Alice Wallenberg Foundation. We thank the Diamond Light Source for access to beamline I09 (proposal number SI35209-1) that contributed to the results presented here. Natalia M. Martin also acknowledges Swedish Research Council (Dnr. 2020-04065) and the StandUp for Energy programme.

REFERENCES

(1) *Best Research-Cell Efficiency Chart*. https://www.nrel.gov/pv/cell-efficiency.html (accessed 2025−02−03)

(2) Schmidt-Mende, L.; Dyakonov, V.; Olthof, S.; Ünlü, F.; Lê, K. M. T.; Mathur, S.; Karabanov, A. D.; Lupascu, D. C.; Herz, L. M.; Hinderhofer, A.; Schreiber, F.; Chernikov, A.; Egger, D. A.; Shargaieva, O.; Cocchi, C.; Unger, E.; Saliba, M.; Byranvand, M. M.; Kroll, M.; Nehm, F.; Leo, K.; Redinger, A.; Höcker, J.; Kirchartz, T.; Warby, J.; Gutierrez-Partida, E.; Neher, D.; Stolterfoht, M.; Würfel, U.; Unmüssig, M.; Herterich, J.; Baretzky, C.; Mohanraj, J.; Thelakkat, M.; Maheu, C.; Jaegermann, W.; Mayer, T.; Rieger, J.; Fauster, T.; Niesner, D.; Yang, F.; Albrecht, S.; Riedl, T.; Fakharuddin, A.; Vasilopoulou, M.; Vaynzof, Y.; Moia, D.; Maier, J.; Franckevičius, M.; Gulbinas, V.; Kerner, R. A.; Zhao, L.; Rand, B. P.; Glück, N.; Bein, T.; Matteocci, F.; Castriotta, L. A.; Di Carlo, A.; Scheffler, M.; Draxl, C. Roadmap on Organic−Inorganic Hybrid Perovskite Semiconductors and Devices. *APL Materials* **2021**, *9* (10), No. 109202.

(3) De Wolf, S.; Holovsky, J.; Moon, S.-J.; Löper, P.; Niesen, B.; Ledinsky, M.; Haug, F.-J.; Yum, J.-H.; Ballif, C. Organometallic Halide Perovskites: Sharp Optical Absorption Edge and Its Relation to Photovoltaic Performance. *J. Phys. Chem. Lett.* **2014**, *5* (6), 1035−1039.

(4) Stranks, S. D.; Eperon, G. E.; Grancini, G.; Menelaou, C.; Alcocer, M. J. P.; Leijtens, T.; Herz, L. M.; Petrozza, A.; Snaith, H. J. Electron-Hole Diffusion Lengths Exceeding 1 Micrometer in an Organometal Trihalide Perovskite Absorber. *Science* **2013**, *342* (6156), 341−344.

(5) Xiang, W.; Liu, S.; Tress, W. A Review on the Stability of Inorganic Metal Halide Perovskites: Challenges and Opportunities for Stable Solar Cells. *Energy Environ. Sci.* **2021**, *14* (4), 2090−2113.

(6) Yan, J.; Savenije, T. J.; Mazzarella, L.; Isabella, O. Progress and Challenges on Scaling up of Perovskite Solar Cell Technology. *Sustain. Energy Fuels* **2022**, *6* (2), 243−266.

(7) Zardetto, V.; Williams, B. L.; Perrotta, A.; Giacomo, F. D.; Verheijen, M. A.; Andriessen, R.; Kessels, W. M. M.; Creatore, M. Atomic Layer Deposition for Perovskite Solar Cells: Research Status. *Sustainable Energy Fuels* **2017**, *1* (1), 30−55.

(8) Seo, S.; Jeong, S.; Park, H.; Shin, H.; Park, N.-G. Atomic Layer Deposition for Efficient and Stable Perovskite Solar Cells. *Chem. Commun.* **2019**, *55* (17), 2403−2416.

(9) Raiford, J. A.; Oyakhire, S. T.; Bent, S. F. Applications of Atomic Layer Deposition and Chemical Vapor Deposition for Perovskite Solar Cells. *Energy Environ. Sci.* **2020**, *13* (7), 1997−2023.

(10) Kim, I. S.; Haasch, R. T.; Cao, D. H.; Farha, O. K.; Hupp, J. T.; Kanatzidis, M. G.; Martinson, A. B. F. Amorphous TiO2 Compact Layers via ALD for Planar Halide Perovskite Photovoltaics. *ACS Appl. Mater. Interfaces* **2016**, *8* (37), 24310−24314.

(11) Hu, T.; Becker, T.; Pourdavoud, N.; Zhao, J.; Brinkmann, K. O.; Heiderhoff, R.; Gahlmann, T.; Huang, Z.; Olthof, S.; Meerholz, K.; Többens, D.; Cheng, B.; Chen, Y.; Riedl, T. Indium-Free Perovskite Solar Cells Enabled by Impermeable Tin-Oxide Electron Extraction Layers. *Adv. Mater.* **2017**, *29* (27), No. 1606656.

(12) Jeong, S.; Seo, S.; Park, H.; Shin, H. Atomic Layer Deposition of a SnO2 Electron-Transporting Layer for Planar Perovskite Solar Cells with a Power Conversion Efficiency of 18.3%. *Chem. Commun.* **2019**, *55* (17), 2433−2436.

(13) Lee, S.-U.; Park, H.; Shin, H.; Park, N.-G. Atomic Layer Deposition of SnO2 Using Hydrogen Peroxide Improves the Efficiency and Stability of Perovskite Solar Cells. *Nanoscale* **2023**, *15* (10), 5044−5052.

(14) Chen, K.-T.; Hsu, C.-H.; Ren, F.-B.; Wang, C.; Gao, P.; Wu, W.-Y.; Lien, S.-Y.; Zhu, W.-Z. Influence of Annealing Temperature of Nickel Oxide as Hole Transport Layer Applied for Inverted Perovskite Solar Cells. *J. Vac. Sci. Technol. A* **2021**, *39* (6), No. 062401.

(15) Koushik, D.; Jošt, M.; Dučinskas, A.; Burgess, C.; Zardetto, V.; Weijtens, C.; Verheijen, M. A.; Kessels, W. M. M.; Albrecht, S.; Creatore, M. Plasma-Assisted Atomic Layer Deposition of Nickel Oxide as Hole Transport Layer for Hybrid Perovskite Solar Cells. *J. Mater. Chem. C* **2019**, *7* (40), 12532−12543.

(16) Jošt, M.; Köhnen, E.; Al-Ashouri, A.; Bertram, T.; Tomšič, Š.; Magomedov, A.; Kasparavicius, E.; Kodalle, T.; Lipovšek, B.; Getautis, V.; Schlatmann, R.; Kaufmann, C. A.; Albrecht, S.; Topič, M. Perovskite/CIGS Tandem Solar Cells: From Certified 24.2% toward 30% and Beyond. *ACS Energy Lett.* **2022**, *7* (4), 1298−1307.

(17) Aydin, E.; Ugur, E.; Yildirim, B. K.; Allen, T. G.; Dally, P.; Razzaq, A.; Cao, F.; Xu, L.; Vishal, B.; Yazmaciyan, A.; Said, A. A.; Zhumagali, S.; Azmi, R.; Babics, M.; Fell, A.; Xiao, C.; De Wolf, S. Enhanced Optoelectronic Coupling for Perovskite/Silicon Tandem Solar Cells. *Nature* **2023**, *623* (7988), 732−738.

(18) Al-Ashouri, A.; Köhnen, E.; Li, B.; Magomedov, A.; Hempel, H.; Caprioglio, P.; Márquez, J. A.; Morales Vilches, A. B.; Kasparavicius, E.; Smith, J. A.; Phung, N.; Menzel, D.; Grischek, M.; Kegelmann, L.; Skroblin, D.; Gollwitzer, C.; Malinauskas, T.; Jošt, M.; Matič, G.; Rech, B.; Schlatmann, R.; Topič, M.; Korte, L.; Abate, A.; Stannowski, B.; Neher, D.; Stolterfoht, M.; Unold, T.; Getautis, V.; Albrecht, S. Monolithic Perovskite/Silicon Tandem Solar Cell with 29% Efficiency by Enhanced Hole Extraction. *Science* **2020**, *370* (6522), 1300−1309.

(19) Lin, R.; Wang, Y.; Lu, Q.; Tang, B.; Li, J.; Gao, H.; Gao, Y.; Li, H.; Ding, C.; Wen, J.; Wu, P.; Liu, C.; Zhao, S.; Xiao, K.; Liu, Z.; Ma, C.; Deng, Y.; Li, L.; Fan, F.; Tan, H. All-Perovskite Tandem Solar Cells with 3D/3D Bilayer Perovskite Heterojunction. *Nature* **2023**, *620* (7976), 994−1000.

(20) Gao, D.; Li, B.; Liu, Q.; Zhang, C.; Yu, Z.; Li, S.; Gong, J.; Qian, L.; Vanin, F.; Schutt, K.; Davis, M. A.; Palmstrom, A. F.; Harvey, S. P.; Long, N. J.; Luther, J. M.; Zeng, X. C.; Zhu, Z. Long-Term Stability in Perovskite Solar Cells through Atomic Layer Deposition of Tin Oxide. *Science* **2024**, *386*, 187.

(21) Chen, H.; Liu, C.; Xu, J.; Maxwell, A.; Zhou, W.; Yang, Y.; Zhou, Q.; Bati, A. S. R.; Wan, H.; Wang, Z.; Zeng, L.; Wang, J.; Serles, P.; Liu, Y.; Teale, S.; Liu, Y.; Saidaminov, M. I.; Li, M.; Rolston, N.; Hoogland, S.; Filleter, T.; Kanatzidis, M. G.; Chen, B.; Ning, Z.; Sargent, E. H. Improved Charge Extraction in Inverted Perovskite Solar Cells with Dual-Site-Binding Ligands. *Science* **2024**, *384* (6692), 189−193.

(22) Brinkmann, K. O.; Zhao, J.; Pourdavoud, N.; Becker, T.; Hu, T.; Olthof, S.; Meerholz, K.; Hoffmann, L.; Gahlmann, T.; Heiderhoff, R.; Oszajca, M. F.; Luechinger, N. A.; Rogalla, D.; Chen, Y.; Cheng, B.; Riedl, T. Suppressed Decomposition of Organometal Halide Perovskites by Impermeable Electron-Extraction Layers in Inverted Solar Cells. *Nat. Commun.* **2017**, *8* (1), No. 13938.

(23) Ye, F.; Zhang, S.; Warby, J.; Wu, J.; Gutierrez-Partida, E.; Lang, F.; Shah, S.; Saglamkaya, E.; Sun, B.; Zu, F.; Shoaee, S.; Wang, H.; Stiller, B.; Neher, D.; Zhu, W.-H.; Stolterfoht, M.; Wu, Y. Overcoming C60-Induced Interfacial Recombination in Inverted Perovskite Solar Cells by Electron-Transporting Carborane. *Nat. Commun.* **2022**, *13* (1), 7454.

(24) Hultqvist, A.; Jacobsson, T. J.; Svanström, S.; Edoff, M.; Cappel, U. B.; Rensmo, H.; Johansson, E. M. J.; Boschloo, G.; Törndahl, T. SnOx Atomic Layer Deposition on Bare Perovskite—An Investigation of Initial Growth Dynamics, Interface Chemistry, and Solar Cell Performance. *ACS Appl. Energy Mater.* **2021**, *4* (1), 510−522.

(25) Bracesco, A. E. A.; Burgess, C. H.; Todinova, A.; Zardetto, V.; Koushik, D.; Kessels, W. M. M.; Dogan, I.; Weijtens, C. H. L.; Veenstra, S.; Andriessen, R.; Creatore, M. The Chemistry and Energetics of the Interface between Metal Halide Perovskite and

https://doi.org/10.1021/acsaem.5c00968
ACS Appl. Energy Mater. 2025, 8, 8467−8478

Atomic Layer Deposited Metal Oxides. *J. Vac. Sci. Technol., A* **2020**, *38* (6), No. 063206.
(26) Mallik, N.; Hajhemati, J.; Frégnaux, M.; Coutancier, D.; Toby, A.; Zhang, S.-T.; Hartmann, C.; Hüsam, E.; Saleh, A.; Vincent, T.; Fournier, O.; Wilks, R. G.; Aureau, D.; Félix, R.; Schneider, N.; Bär, M.; Schulz, P. Interface Defect Formation for Atomic Layer Deposition of SnO2 on Metal Halide Perovskites. *Nano Energy* **2024**, *126*, No. 109582.
(27) Das, C.; Kot, M.; Hellmann, T.; Wittich, C.; Mankel, E.; Zimmermann, I.; Schmeisser, D.; Khaja Nazeeruddin, M.; Jaegermann, W. Atomic Layer-Deposited Aluminum Oxide Hinders Iodide Migration and Stabilizes Perovskite Solar Cells. *Cell Rep. Phys. Sci.* **2020**, *1* (7), No. 100112.
(28) Artuk, K.; Turkay, D.; Mensi, M. D.; Steele, J. A.; Jacobs, D. A.; Othman, M.; Yu Chin, X.; Moon, S.-J.; Tiwari, A. N.; Hessler-Wyser, A.; Jeangros, Q.; Ballif, C.; Wolff, C. M. A Universal Perovskite/C60 Interface Modification via Atomic Layer Deposited Aluminum Oxide for Perovskite Solar Cells and Perovskite-Silicon Tandems. *Adv. Mater.* **2024**, *36* (21), No. 2311745.
(29) Kot, M.; Das, C.; Wang, Z.; Henkel, K.; Rouissi, Z.; Wojciechowski, K.; Snaith, H. J.; Schmeisser, D. Room-Temperature Atomic Layer Deposition of Al2O3: Impact on Efficiency, Stability and Surface Properties in Perovskite Solar Cells. *ChemSusChem* **2016**, *9* (24), 3401−3406.
(30) Ünlü, F.; Jung, E.; Haddad, J.; Kulkarni, A.; Öz, S.; Choi, H.; Fischer, T.; Chakraborty, S.; Kirchartz, T.; Mathur, S. Understanding the Interplay of Stability and Efficiency in A-Site Engineered Lead Halide Perovskites. *APL Materials* **2020**, *8* (7), No. 070901.
(31) LaFollette, D. K.; Hidalgo, J.; Allam, O.; Yang, J.; Shoemaker, A.; Li, R.; Lai, B.; Lawrie, B.; Kalinin, S.; Perini, C. A. R.; Ahmadi, M.; Jang, S. S.; Correa-Baena, J.-P. Bromine Incorporation Affects Phase Transformations and Thermal Stability of Lead Halide Perovskites. *J. Am. Chem. Soc.* **2024**, *146* (27), 18576−18585.
(32) Lee, J.-W.; Tan, S.; Seok, S. I.; Yang, Y.; Park, N.-G. Rethinking the A Cation in Halide Perovskites. *Science* **2022**, *375* (6583), No. eabj1186.
(33) Azmi, R.; Utomo, D. S.; Vishal, B.; Zhumagali, S.; Dally, P.; Risqi, A. M.; Prasetio, A.; Ugur, E.; Cao, F.; Imran, I. F.; Said, A. A.; Pininti, A. R.; Subbiah, A. S.; Aydin, E.; Xiao, C.; Seok, S. I.; De Wolf, S. Double-Side 2D/3D Heterojunctions for Inverted Perovskite Solar Cells. *Nature* **2024**, *628* (8006), 93−98.
(34) Liu, J.; He, Y.; Ding, L.; Zhang, H.; Li, Q.; Jia, L.; Yu, J.; Lau, T. W.; Li, M.; Qin, Y.; Gu, X.; Zhang, F.; Li, Q.; Yang, Y.; Zhao, S.; Wu, X.; Liu, J.; Liu, T.; Gao, Y.; Wang, Y.; Dong, X.; Chen, H.; Li, P.; Zhou, T.; Yang, M.; Ru, X.; Peng, F.; Yin, S.; Qu, M.; Zhao, D.; Zhao, Z.; Li, M.; Guo, P.; Yan, H.; Xiao, C.; Xiao, P.; Yin, J.; Zhang, X.; Li, Z.; He, B.; Xu, X. Perovskite/Silicon Tandem Solar Cells with Bilayer Interface Passivation. *Nature* **2024**, *635* (8039), 596−603.
(35) Hossain, K.; Kulkarni, A.; Bothra, U.; Klingebiel, B.; Kirchartz, T.; Saliba, M.; Kabra, D. Resolving the Hydrophobicity of the Me-4PACz Hole Transport Layer for Inverted Perovskite Solar Cells with Efficiency 20%. *ACS Energy Lett.* **2023**, *8* (9), 3860−3867.
(36) Scofield, J. H. *Theoretical Photoionization Cross Sections from 1 to 1500 keV.*; UCRL-51326; Lawrence Livermore Laboratory, 1973. .
(37) Stoumpos, C. C.; Malliakas, C. D.; Kanatzidis, M. G. Semiconducting Tin and Lead Iodide Perovskites with Organic Cations: Phase Transitions, High Mobilities, and Near-Infrared Photoluminescent Properties. *Inorg. Chem.* **2013**, *52* (15), 9019−9038.
(38) Hanusch, F. C.; Wiesenmayer, E.; Mankel, E.; Binek, A.; Angloher, P.; Fraunhofer, C.; Giesbrecht, N.; Feckl, J. M.; Jaegermann, W.; Johrendt, D.; Bein, T.; Docampo, P. Efficient Planar Heterojunction Perovskite Solar Cells Based on Formamidinium Lead Bromide. *J. Phys. Chem. Lett.* **2014**, *5* (16), 2791−2795.
(39) Eperon, G. E.; Stranks, S. D.; Menelaou, C.; Johnston, M. B.; Herz, L. M.; Snaith, H. J. Formamidinium Lead Trihalide: A Broadly Tunable Perovskite for Efficient Planar Heterojunction Solar Cells. *Energy Environ. Sci.* **2014**, *7* (3), 982−988.
(40) Amat, A.; Mosconi, E.; Ronca, E.; Quarti, C.; Umari, P.; Nazeeruddin, Md. K.; Grätzel, M.; De Angelis, F. Cation-Induced Band-Gap Tuning in Organohalide Perovskites: Interplay of Spin-Orbit Coupling and Octahedra Tilting. *Nano Lett.* **2014**, *14* (6), 3608−3616.
(41) Mannino, G.; Deretzis, I.; Smecca, E.; La Magna, A.; Alberti, A.; Ceratti, D.; Cahen, D. Temperature-Dependent Optical Band Gap in CsPbBr 3, MAPbBr3, and FAPbBr3 Single Crystals. *J. Phys. Chem. Lett.* **2020**, *11* (7), 2490−2496.
(42) Zuo, L.; Yao, J.; Li, H.; Chen, H. Assessing the Origin of the S-Shaped I-V Curve in Organic Solar Cells: An Improved Equivalent Circuit Model. *Sol. Energy Mater. Sol. Cells* **2014**, *122*, 88−93.
(43) Yu, F.; Liang, Y.; Sun, X.; Huang, G.; Xu, C. Modelling Solar Cells' S-Shaped *I-V* Characteristics with an Analytical Solution to Lumped-Parameter Equivalent Circuit Model. *Sol. Energy* **2020**, *202*, 498−506.
(44) Li, N.; Cheng, C.; Wei, H.; Liu, H.; Li, X.; Li, W.; Wang, L. Enhanced Efficiency and Stability of Inverted Perovskite Solar Cells by Interfacial Engineering with Alkyl Bisphosphonic Molecules. *RSC Adv.* **2017**, *7* (67), 42105−42112.
(45) Li, W.; Li, J.; Niu, G.; Wang, L. Effect of Cesium Chloride Modification on the Film Morphology and UV-Induced Stability of Planar Perovskite Solar Cells. *J. Mater. Chem. A* **2016**, *4* (30), 11688−11695.
(46) Chistiakova, G.; Mews, M.; Wilks, R. G.; Bär, M.; Korte, L. In-System Photoelectron Spectroscopy Study of Tin Oxide Layers Produced from Tetrakis(Dimethylamino)Tin by Plasma Enhanced Atomic Layer Deposition. *J. Vac. Sci. Technol. A* **2018**, *36* (2), No. 02D401.
(47) Martin, N. M.; Babucci, M.; Stolt, L.; Hultqvist, A.; Kokkonen, E.; Timm, R.; Schnadt, J.; Platzer-Björkman, C.; Törndahl, T. In Situ Studies of Atomic Layer Deposition of Hafnium Oxide on (Ag,Cu)(In,Ga)Se2 for Thin Film Solar Cells. *ACS Appl. Energy Mater.* **2025**, *8*, 461.
(48) Mackus, A. J. M.; MacIsaac, C.; Kim, W.-H.; Bent, S. F. Incomplete Elimination of Precursor Ligands during Atomic Layer Deposition of Zinc-Oxide, Tin-Oxide, and Zinc-Tin-Oxide. *J. Chem. Phys.* **2017**, *146* (5), No. 052802.
(49) Palmstrom, A. F.; Raiford, J. A.; Prasanna, R.; Bush, K. A.; Sponseller, M.; Cheacharoen, R.; Minichetti, M. C.; Bergsman, D. S.; Leijtens, T.; Wang, H.; Bulović, V.; McGehee, M. D.; Bent, S. F. Interfacial Effects of Tin Oxide Atomic Layer Deposition in Metal Halide Perovskite Photovoltaics. *Adv. Energy Mater.* **2018**, *8* (23), No. 1800591.
(50) Juarez-Perez, E. J.; Ono, L. K.; Qi, Y. Thermal Degradation of Formamidinium Based Lead Halide Perovskites into Sym-Triazine and Hydrogen Cyanide Observed by Coupled Thermogravimetry-Mass Spectrometry Analysis. *J. Mater. Chem. A* **2019**, *7* (28), 16912−16919.
(51) Bracesco, A. E. A.; Jansen, J. W. P.; Xue, H.; Zardetto, V.; Brocks, G.; Kessels, W. M. M.; Tao, S.; Creatore, M. In Situ IR Spectroscopy Studies of Atomic Layer-Deposited SnO2 on Formamidinium-Based Lead Halide Perovskite. *ACS Appl. Mater. Interfaces* **2023**, *15* (31), 38018−38028.
(52) Ma, H.; Jia, Y.; Zhu, G.; Zhang, F.; Rhee, S.; Lee, B.; Liu, C. Study of Cyano and Hydroxyl Groups Modification on the Properties of Porous Carbon Nitride Synthesized by Using a Salt Assistant Method. *Appl. Surf. Sci.* **2020**, *507*, No. 144885.
(53) Ahuja, R.; Arwin, H.; Ferreira da Silva, A.; Persson, C.; Osorio-Guillén, J. M.; Souza de Almeida, J.; Moyses Araujo, C.; Veje, E.; Veissid, N.; An, C. Y.; Pepe, I.; Johansson, B. Electronic and Optical Properties of Lead Iodide. *J. Appl. Phys.* **2002**, *92* (12), 7219−7224.
(54) Sohrabpoor, H.; Elyasi, M.; Aldosari, M.; Gorji, N. E. Modeling the PbI2 Formation in Perovskite Solar Cells Using XRD/XPS Patterns. *Superlattices Microstruct.* **2016**, *97*, 556−561.
(55) Binek, A.; Hanusch, F. C.; Docampo, P.; Bein, T. Stabilization of the Trigonal High-Temperature Phase of Formamidinium Lead Iodide. *J. Phys. Chem. Lett.* **2015**, *6* (7), 1249−1253.

https://doi.org/10.1021/acsaem.5c00968
ACS Appl. Energy Mater. 2025, 8, 8467−8478

(56) Han, Q.; Bae, S.-H.; Sun, P.; Hsieh, Y.-T.; Yang, Y.; Rim, Y. S.; Zhao, H.; Chen, Q.; Shi, W.; Li, G.; Yang, Y. Single Crystal Formamidinium Lead Iodide (FAPbI3): Insight into the Structural, Optical, and Electrical Properties. *Adv. Mater.* **2016**, *28* (11), 2253−2258.
(57) Liang, Y.; Li, F.; Cui, X.; Lv, T.; Stampfl, C.; Ringer, S. P.; Yang, X.; Huang, J.; Zheng, R. Toward Stabilization of Formamidinium Lead Iodide Perovskites by Defect Control and Composition Engineering. *Nat. Commun.* **2024**, *15* (1), 1707.

https://doi.org/10.1021/acsaem.5c00968
ACS Appl. Energy Mater. 2025, 8, 8467−8478